RSC Advances

PAPER

View Article Online
View Journal | View Issue

Cite this: *RSC Adv.*, 2023, **13**, 12483

Activation of peroxymonosulfate by palygorskite supported Co–Fe for water treatment

Wenxiang Xia,[a] Qianqian Wu,[a] Rui Huang,[b] Yinglu Tao,[a] Kaimei Wang,[a] Shuxiao Wu,[a] Songxue Wang, *[a] Mingli Wang[c] and Qingsheng Li[d]

Received 13th December 2022
Accepted 16th April 2023

DOI: 10.1039/d2ra07948h

rsc.li/rsc-advances

In the present work, palygorskite (PAL) supported Co–Fe oxides (CoFe@PAL) were prepared and used as a peroxymonosulfate (PMS) activator for removal of rhodamine B (RhB) in water. The results showed that CoFe@PAL prepared at impregnation solution of 50 g L^{-1} and calcination temperature of 500 °C showed the best catalytic performance. The removal efficiency of RhB (10 mg L^{-1}) by PMS (0.1 mmol L^{-1}) activated with CoFe@PAL (1 g L^{-1}) was above 98% within 60 min. The effects of various environmental factors including initial pH, humic acid (HA) and inorganic anions on the removal effect were simultaneously investigated. The radical quenching experiments and EPR characterization revealed that $^{\bullet}OH$, $SO_4^{\bullet-}$, $O_2^{\bullet-}$ and $^1O_2$ radicals existed in the CoFe@PAL/PMS system simultaneously. The intermediates during RhB degradation were analyzed by LC-MS and possible degradation pathways of RhB were proposed. Moreover, CoFe@PAL exhibited superior stability and reusability.

1. Introduction

Organic dye wastewater, which is extensively emitted by production processes in the textile, cosmetic, paint, and plastic industries, poses a threat to both the environment and human health due to its deep chromaticity, complex organic compositions, high chemical oxygen demand (COD) concentration and recalcitrance.[1,2] Traditional water treatment processes, including adsorption[3] and biological degradation,[4] generally suffer from low efficiency of removal or degradation. Advanced oxidation processes (AOPs) based on the hydroxyl radical ($^{\bullet}OH$) are efficient water treatment technologies for removing high organic loading wastewater.[5,6] Compared with traditional $^{\bullet}OH$ based AOPs, $SO_4^{\bullet-}$ based AOPs exhibit higher redox potential, longer lifespan and wider pH range.[7,8] Recently, peroxymonosulfate (PMS) activation, as a novel developing AOPs, has attracted increasing attention from researchers across the globe.

Persulfates activation by transition metals is one of the most efficient methods with simple operation and low energy consumption.[9,10] For example, homogeneous Co^{2+} is considered to be the most efficient PMS activator for transition metals.[11,12] However, cobalt ions pose some problems, such as separation difficulties and significant biotoxicity. So considerable researchers have been committed to develop heterogeneous Co-based catalysts including Co_3O_4 and Co oxides/carbon composites, which could effectively reduce toxic contamination and improve the stability of the catalyst.[13,14] Furthermore, some studies showed that some transition metals such as Fe, Cu, and Mn doping into the Co-based catalyst can significantly improve the activation performance of persulfates.[15,16] Therefore, some researchers have exploited bimetallic multiphase catalysts to promote persulfates activation and enhance catalyst stability. Li[8] and co-workers prepared $Co_{0.8}Fe_{2.2}O_4$ nanocatalysts for PMS activation and found that the catalytic activity of $Co_{0.8}Fe_{2.2}O_4$ was superior to Fe_3O_4 and Co_3O_4. Therefore, the incorporation of other metal components into a single metal oxide is benefit for the catalytic activity of PMS.

However, the application of metal oxide catalysts is greatly limited by agglomeration, few active sites, and a limited surface area.[17,18] Therefore, supported metal oxide catalysts have been extensively studied in the field of wastewater treatment.[19,20] Loading metal oxides onto materials with a large specific surface area can increase the distribution density of the active sites, thus improving the catalytic activity of the catalyst.[21] Palygorskite (PAL) is a natural mineral with a thin sheet structure. Owing to its low price, large specific surface area, and strong chemical stability, PAL has been developed as a support for loading metallic nanoparticles.[22,23] Li[24] and co-workers synthesized MoS_2/PAL *via* a hydrothermal method and applied in the reduction of 4-nitrophenol, the results proved that MoS_2/PAL could prevent the agglomeration of MoS_2 nanoparticles, and its catalytic activity was more excellent than MoS_2.

[a]*School of Environmental and Municipal Engineering, Qingdao University of Technology, Qingdao 266520, China. E-mail: songxue.wang@outlook.com*
[b]*Guangdong GDH Water Co. Ltd, Shenzhen 518021, China*
[c]*Shandong Provincial Qingdao Eco-environment Monitoring Center, Qingdao 266003, China*
[d]*Fujian Provincial Key Laboratory of Marine Ecological Conservation and Restoration, Xiamen 361005, China*

In this study, various common metal salt solutions were selected as precursors, and different bimetallic oxides were loaded onto PAL through impregnation–calcination method. The microscopic morphology and crystallographic structure of catalysts were characterized by SEM, XRD, and BET. The optimal catalyst was used to activate PMS and degrade rhodamine B (RhB) solution. The effects of some important experimental conditions on the catalytic degradation process were investigated. The main active species in the catalytic system were explored, and the stability and reusability of the catalysts were also evaluated. These studies are intended to provide a reference for the treatment of dye wastewater with persulfate.

2. Materials and methods

2.1 Materials and chemicals

The palygorskite (PAL, 0.35–0.45 mm) used was obtained from Jiangsu Meishibo Co., Ltd (China). Peroxymonosulfate (PMS, $KHSO_5 \cdot 0.5KHSO_4 \cdot 0.5K_2SO_4$) was purchased from Shanghai Macklin Biochemistry Technology Co., Ltd (China). Cobalt nitrate hexahydrate ($Co(NO_3)_2 \cdot 6H_2O$), iron nitrate nonahydrate ($Fe(NO_3)_3 \cdot 9H_2O$), copper nitrate trihydrate ($Cu(NO_3)_2 \cdot 3H_2O$), manganese chloride tetrahydrate ($MnCl_2 \cdot 4H_2O$), rhodamine B (RhB), methanol (MeOH) and *tert*-butyl alcohol (TBA) were purchased from Sinopharm Chemical Reagent Co., Ltd (China). All solutions used in the experiments were prepared using deionized (DI) water.

2.2 Sample preparation

The PAL was sonicated in DI water for 30 min and washed several times to remove impurities from the PAL surface, and then the PAL was dried in an oven at 70 °C for 8 h. After drying, the PAL was sealed in a sample bag for later use. 5 g of $Co(NO_3)_2 \cdot 6H_2O$ and $Fe(NO_3)_3 \cdot 9H_2O$ were dissolved in 100 mL of DI water to prepare the precursor solution, and then PAL (15 g) was immersed in this precursor solution for 24 h. Removing the PAL from the solution and drying in an oven at 70 °C for 8 h. The soaked PAL was calcined in a muffle furnace at 500 °C for 3 h and the resultant catalyst was labeled as CoFe@PAL. The same method was used to prepare the CoCu@PAL, CoMn@PAL, FeCu@PAL and FeMn@PAL catalysts.

In addition, a series of CoFe@PAL prepared at different calcination temperatures and different concentrations of impregnation solution were denoted as *x*CoFe@PAL-*y*, where *x* and *y* stand for the calcination dosage of metal salt in the impregnation solution and temperature, respectively.

2.3 Characterization

The microstructure and surface elemental distribution of the samples were analyzed by a field emission scanning electron microscopy (FE-SEM) (SIGMA300, Zeiss, Germany) equipped with energy dispersive spectrometer (EDS). The crystal structure of the samples was analyzed by X-ray diffractometry (XRD) (Smartlab 9 kW, Rigaku, Japan). The elemental information (Fe and Co) of samples was determined by X-ray Photoelectron Spectroscopy (XPS) (ESCALAB 250Xi, Thermo Scientific, USA). The Brunauer–Emmett–Teller (BET) specific surface area and pore size distributions of the samples were analyzed on a Micromeritics ASAP 2460 instrument. The generated reactive radicals in the system were detected by Electron paramagnetic resonance (EPR) (Bruker A300 spectrometer, Germany).

2.4 Experiment procedures

The adsorption and degradation experiments were performed on a magnetic stirrer. A total of 5 mL of 200 mg per L RhB dye was dissolved in 100 mL DI water as the feed solution. Subsequently, the oxidant PMS and catalyst were added and then mixed evenly by stirring with a magnetic stirrer. A certain amount of water sample was collected at a certain time and filtered through 0.22 μm filter, and then detected the absorbance of the samples at $\lambda = 554$ nm on a UV-vis spectrophotometer (UV5800H, China). RhB concentration is proportional to the absorbance at the corresponding wavelength, and the degradation rate of RhB is calculated using the following equation:

$$D(\%) = \frac{A_0 - A_t}{A_0} \times 100 \quad (1)$$

where D is the degradation rate of RhB; A_0 is the initial RhB absorbance; A_t is the RhB absorbance at time t; t is the reaction time, min.

The apparent first-order-rate constants was calculated as follows:

$$\ln \frac{C_t}{C_0} = -kt \quad (2)$$

where C_0 is the initial RhB concentration, mg L^{-1}; C_t is the RhB concentration at time t, mg L^{-1}; t is the reaction time, min; and k is the rate constant of the pseudo-first-order reaction, min^{-1}.

3. Results and discussion

3.1 Characterization of CoFe@PAL

Fig. 1 shows the SEM images of PAL and CoFe@PAL prepared at different calcination temperatures. From the SEM images of PAL at low and high magnification, the surface of PAL was consisted of flat fibers, and most of them were gathered into clusters. Compared to PAL, the surface of CoFe@PAL showed weak fiber structure and abundant pores (Fig. 1b–d), some spheres and sheets of nanoparticles were distributed on the surface of CoFe@PAL, indicating the successful loading of Co and Fe species.[25] Specifically, few nanoparticles were observed on the surface of 5CoFe@PAL-400, while a lot of nanoparticles were uniformly distributed on the surface of 5CoFe@PAL-500. When the prepared temperature reached 600 °C, the size of nanoparticles on the surface of 5CoFe@PAL-600 further increased, due to nanoparticles accumulating with each other at a high temperature.[26]

The EDS spectrum images of 5CoFe@PAL-500 were presented in Fig. 2, showing that 5CoFe@PAL-500 is composed of C, O, Al, Mg, Si, Co and Fe element. Among them, the proportion of Co and Fe was 1.14% and 7.95%, respectively. In

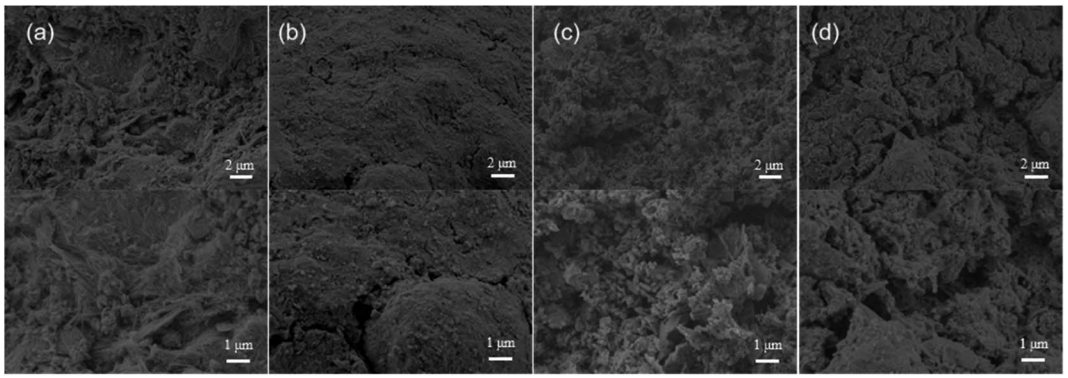

Fig. 1 SEM images of (a) PAL (a), 5CoFe@PAL-400 (b), 5CoFe@PAL-500 (c) and 5CoFe@PAL-600 (d).

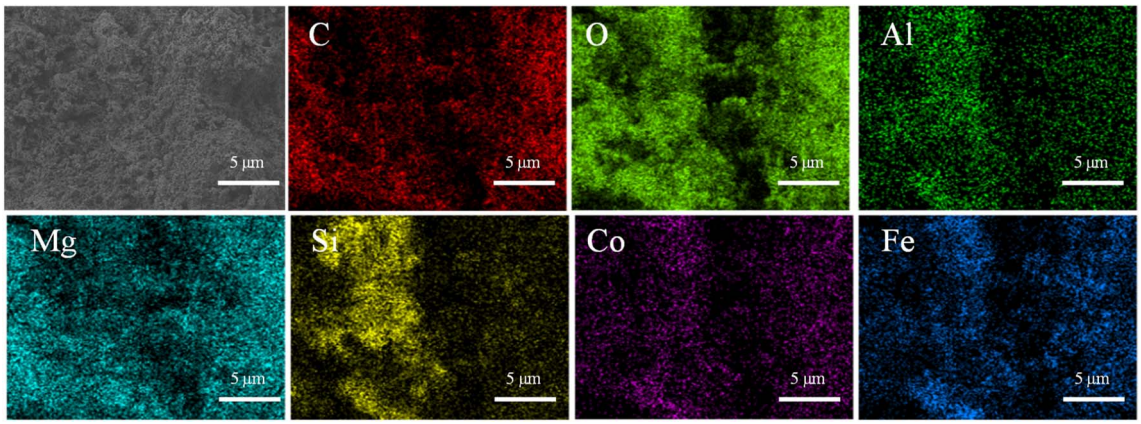

Fig. 2 Element distribution of CoFe@PAL-500.

addition, distribution maps of elements confirmed that each element was uniformly distributed in the 5CoFe@PAL-500.

Further, XRD spectra of PAL and CoFe@PAL are shown in Fig. 3. The diffraction peaks at 26.62° and 60.04° corresponding to (011) and (121) were well indexed to SiO_2, proving that SiO_2 is the component of PAL. Moreover, the XRD patterns of all samples demonstrate almost the same characteristic reflections at 2θ = 24.08°, 33.50°, 36.52°, 41.08°, 44.88°, 51.02°, 60.08°, 63.48°, 67.48° and 87.88°, all of which can be perfectly indexed to dolomite (PDF#75-1654). These results indicated that the type of PAL used in this study is dolomitic palygorskite (palygorskite ≥ 20%, dolomite ≥ 40%). However, no diffraction peaks of Co or Fe species were detected, probably due to other peaks being too strong in the spectra.[27] Additionally, the weaker diffraction intensity of CoFe@PAL as the calcination temperature increased may be attributed to the partial collapse of the PAL structure by high temperatures.[28]

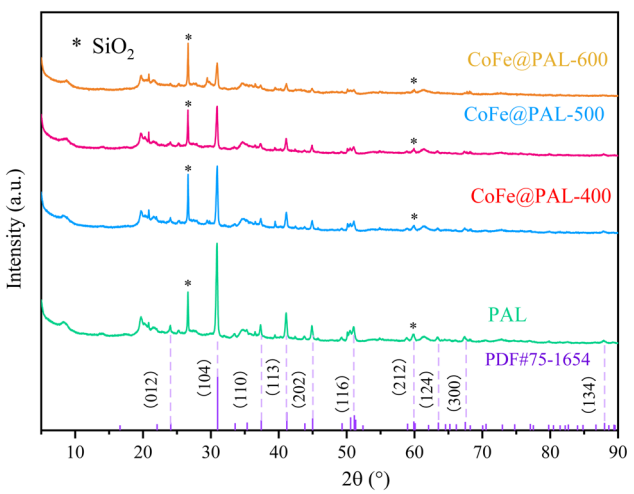

Fig. 3 XRD patterns of PAL, 5CoFe@PAL-400, 5CoFe@PAL-500 and 5CoFe@PAL-600.

The XPS spectra of Fig. 4 show the chemical composition and valence state of CoFe@PAL catalyst. As shown in Fig. 4a, the full survey spectrum of catalyst revealed the presence of Co and Fe elements with the peak at 778.1 eV (Co 2p) and 706.1 eV (Fe 2p). The high-resolution spectra of Fe 2p and Co 2p are presented in Fig. 4b and c. As shown in Fig. 4b, the doublets of Fe $2p_{3/2}$ binding energies at 710.99 eV and Fe $2p_{1/2}$ binding energies at 724.08 eV were due to the contributions from Fe^{3+} ions in octahedral sites, and the doublets of Fe $2p_{3/2}$ binding energies at 713.00 eV and Fe $2p_{1/2}$ binding energies at 725.80 eV were due to the contributions from Fe^{3+} ions in tetrahedral sites.[29] The

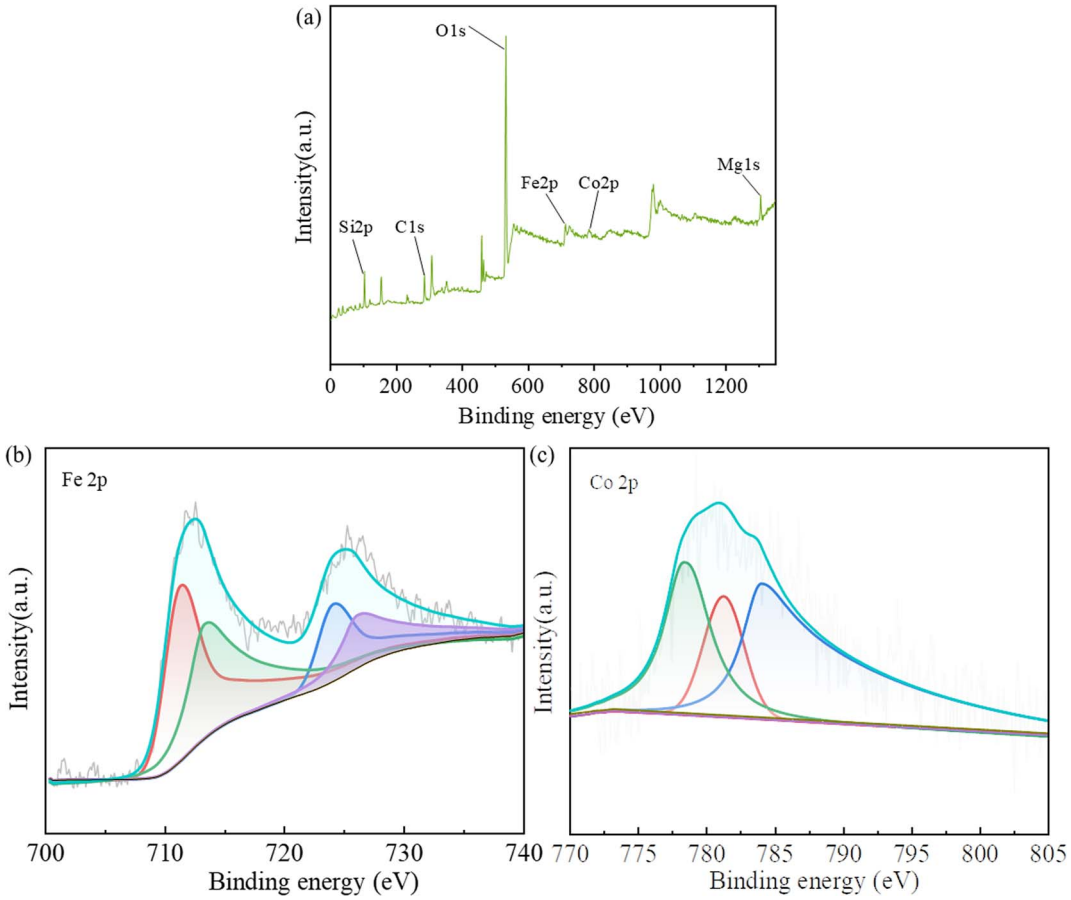

Fig. 4 (a) XPS full survey spectrum, (b) Fe 2p spectrum and (c) Co 2p spectrum of 5CoFe@PAL-500.

XPS spectrum of Co 2p in CoFe@PAL (Fig. 4c) shows three peaks (779.06, 780.92 and 783.90 eV), which could be assigned to Co^{2+} ions in octahedral sites, tetrahedral sites and Co^{3+} ions in octahedral sites.[8] The above results suggested that Fe(III), Co(III) and Co(II) are present on the surface of CoFe@PAL.

The BET specific surface area and pore size distributions of the materials were analyzed, and the results were shown in Fig. 5. According to IUPAC, all the samples exhibited a type IV isotherms with H3-type hysteresis loops, which indicated the presence of mesopores in PAL particles.[19]

As shown in Fig. 5a, with calcining temperature rise, the specific surface area (SSA) of CoFe@PAL increased at first and then decreased; the CoFe@PAL-500 sample exhibited the highest specific surface area (109.97 $m^2 g^{-1}$) among all samples. In Fig. 5b, the average pore size of the catalysts showed a downward trend. The average pore size of 5CoFe@PAL-600 was 50.1 nm, which was smaller than that of 5CoFe@PAL-500 (56.6 nm) and 5CoFe@PAL-400 (60.4 nm). Compared with the PAL, the Co–Fe substance of the precursor solution gradually decomposed at 400 °C and 500 °C. Then the active particles were formed and dispersed on the carrier, leading to improve the specific surface area of CoFe@PAL slightly. However, agglomeration occurred among active particles at 600 °C, and the pores of the carrier were blocked by the agglomerated particles, resulting to the reduction of specific surface area and pore size, which is in accordance with the SEM results.

Fig. 5c and d show the effect of impregnation concentration on CoFe@PAL surface structure. As shown in Fig. 5c, the increasing impregnation concentration of catalysts caused a great increase in the specific surface area. The specific surface area of 8CoFe@PAL-500 reached 121.64 $m^2 g^{-1}$, due to the excess Co and Fe species were accumulated on the surface of catalyst. From Fig. 5d, the average pore size of PAL, 2CoFe@PAL-500 and 8CoFe@PAL-500 was 69.7 nm, 70.7 nm and 69.0 nm, respectively, showing no significant difference. However, the average pore size of 5CoFe@PAL-500 decreased to 56.6 nm obviously. Combined with the SEM image in Fig. 1c, a lot of active component particles on the surface of 5CoFe@PAL-500 filled and covered the small pores in PAL, resulting in a smaller pore size.

3.2 Catalytic performance of CoFe@PAL

In this study, five kinds of combinations of Co–Fe, Co–Mn, Co–Cu, Fe–Mn and Fe–Cu were selected to prepare catalysts. The catalytic performance of these coated samples was investigated by activating PMS to remove RhB. As shown in Fig. 6, the removal efficiency of RhB by PMS alone was only 5.54% after reacting for 60 min, revealing its negligible degradation

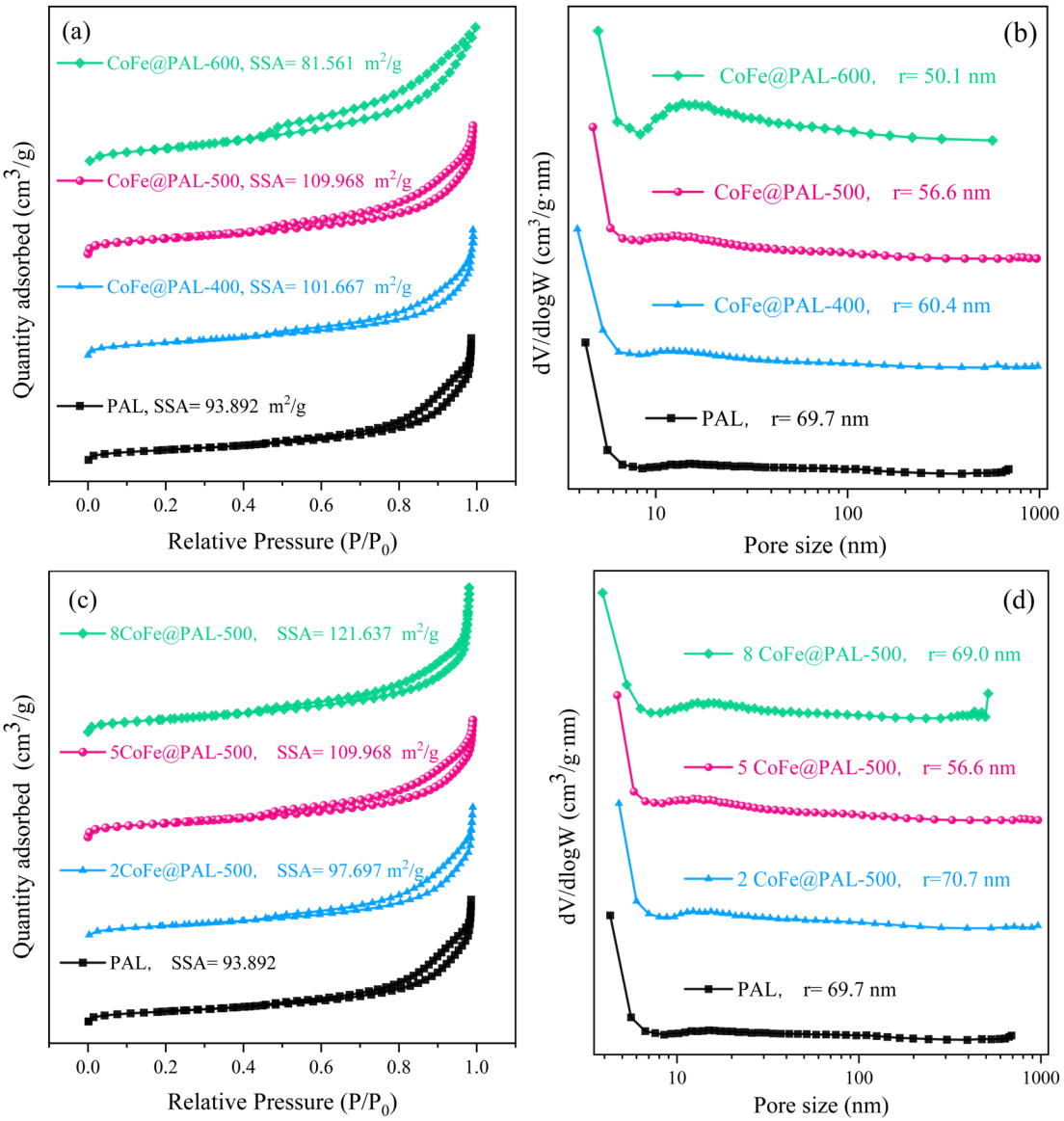

Fig. 5 (a and c) N_2 adsorption–desorption isotherms and (b and d) the corresponding pore size distributions of catalysts (SSA: specific surface area, *r*: average pore size).

capacity. The adsorption efficiency of RhB by PAL alone was 13.01%, indicating that only a tiny amount of RhB can be adsorbed by PAL. The simultaneous presence of PAL and PMS enhanced the removal efficiency of RhB with a removal efficiency of 22.84%. When the CoFe@PAL, CoMn@PAL, CoCu@PAL, FeMn@PAL, and FeCu@PAL was individually added to the PMS/RhB mixed solution, the removal rate of RhB reached 94.28%, 73.11%, 53.13%, 43.54% and 29.35%, respectively. These results indicate that CoFe@PAL presented the excellent performance on activating PMS to remove RhB, and the synergistic effect of adsorption and PMS activation accelerated the removal efficiency.

Considering the influence of preparation conditions, the effects of calcination temperature and impregnation concentration on RhB degradation were evaluated and the results are shown in Fig. 7. In Fig. 7a, the adsorption effect of PAL, CoFe@PAL-400 and CoFe@PAL-500 on RhB was 13.10%, 14.01% and 14.53%, respectively. However, the adsorption removal of RhB decreased, when the preparation temperature increased to 600 °C. Combined with BET characterization analysis, the specific surface area of CoFe@PAL-600 was significantly lower than that of the other three samples, which resulted in a lower adsorption performance. After adsorption experiments, the removal effects of RhB were studied in the presence of CoFe@PAL and PMS, as shown in Fig. 7a. To be specific, RhB was almost completely removed within 50 min in the CoFe@PAL-400/PMS system. However, about 94.28% and 79.90% RhB were degraded within 60 min in CoFe@PAL-500/PMS and CoFe@PAL-600/PMS systems, respectively. The apparent rate constant (k) of CoFe@PAL-400/PMS system was 0.029 min^{-1}, which was much higher than that of other catalytic systems. Thus, the activity performance of CoFe@PAL was

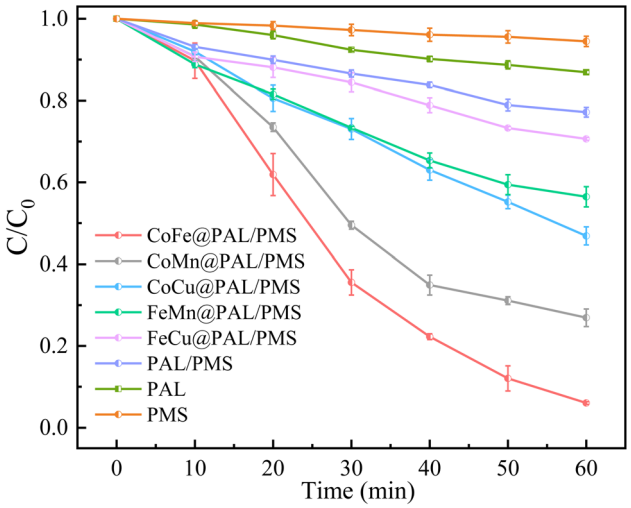

Fig. 6 RhB removal performance in different systems ($[RhB]_0$ = 10 mg L^{-1}, $[PMS]_0$ = 0.1 mM, [catalyst] = 1 g L^{-1}).

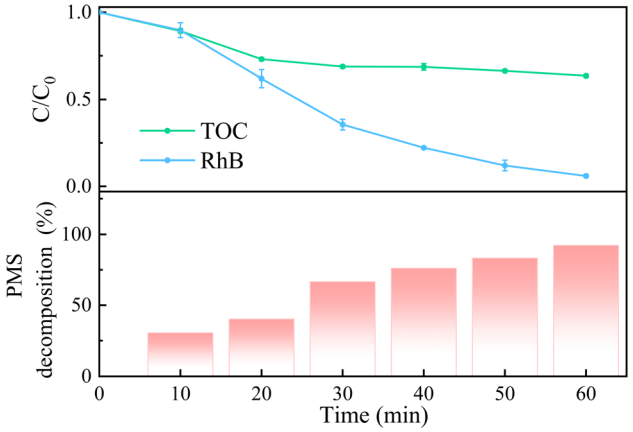

Fig. 8 TOC removal rate, RhB degradation rate and PMS decomposition rate in the 5CoFe@PAL-500/PMS system ([catalyst] = 1 g L^{-1}, $[PMS]_0$ = 0.1 mM, $[RhB]_0$ = 10 mg L^{-1}).

affected by its calcination temperature, and CoFe@PAL-400 showed the best catalytic activation.

The leaching of metal ions from the catalyst/PMS system can cause secondary contamination to the environment. In this study, the leaching of Co and Fe was detected by ICP-OES in different systems. As shown in Fig. 7b, the amount of dissolved Co ion in the CoFe@PAL-400/PMS system was 22.29 μg L^{-1}. The amounts of dissolved Co ion decreased as calcination temperature increased from 400 °C to 600 °C. The precursor solution

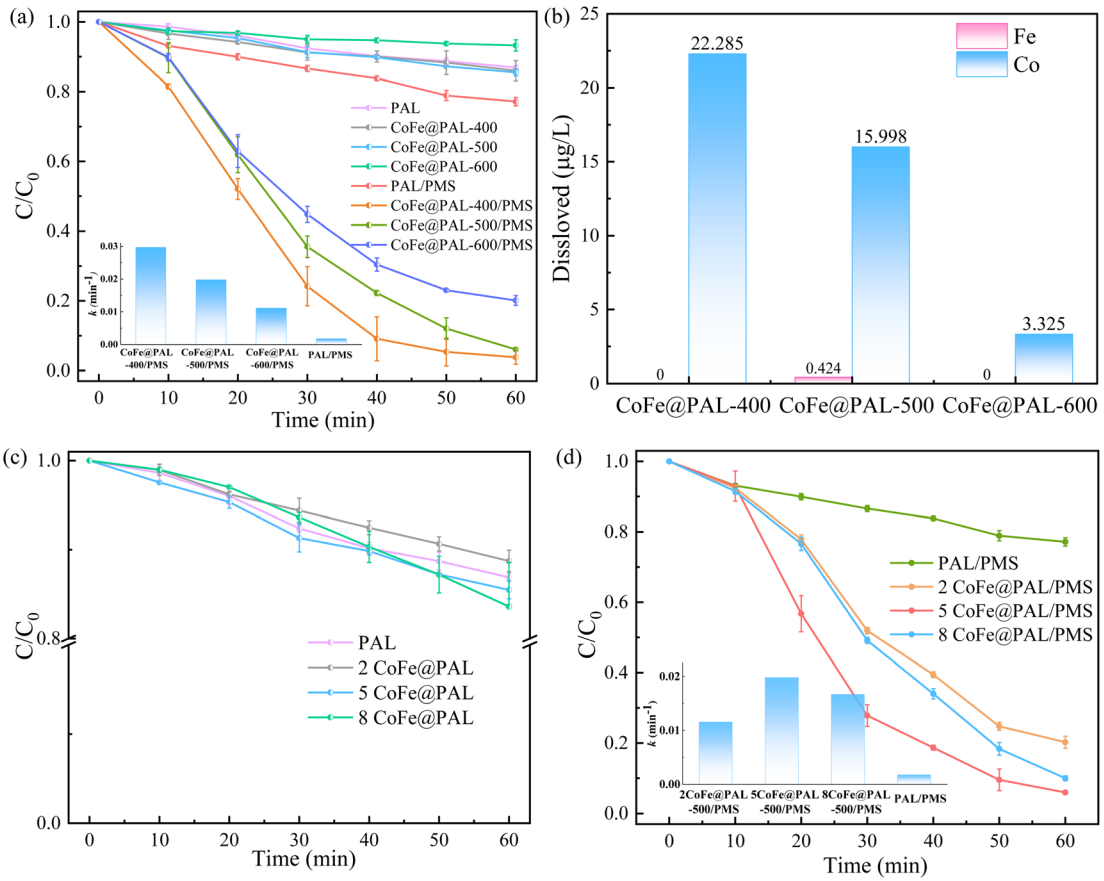

Fig. 7 (a) Effect of calcination temperature of catalyst on RhB removal, (b) the amount of metal dissolved in different systems, (c) effect of impregnation concentration of catalyst on RhB adsorption, (d) effect of impregnation concentration of catalyst on RhB degradation ([catalyst] = 1 g L^{-1}, $[PMS]_0$ = 0.1 mM, $[RhB]_0$ = 10 mg L^{-1}).

on the surface of support was not completely oxidized to metal oxides at low calcination temperature, leading to the residual metal salts leaching in water to produce Co ions. In addition, the concentration of leached Fe in the CoFe@PAL-500/PMS system was only 0.43 μg L^{-1}, which was conformed to the discharge standard of iron.[30] Therefore, CoFe@PAL-500, which dissolved a relatively low amount of Co ions, was selected for follow-up tests.

Fig. 7 illustrates the influence of impregnation concentration on RhB removal. Fig. 7c presented that adsorption efficiencies of RhB were 16.40%, 14.53%, and 11.27% by 8CoFe@PAL-500, 5CoFe@PAL-500, 2CoFe@PAL-500, respectively. Characterization analysis based on BET showed the specific surface area of 2CoFe@PAL-500 was 96.70 m^2 g^{-1}, smaller than those of 5CoFe@PAL-500 (109.97 m^2 g^{-1}) and 8CoFe@PAL-500 (121.64 m^2 g^{-1}). The higher specific area provided more adsorption sites for the reaction, which was conducive to enhancing the adsorption performance of catalyst.

Fig. 7d shows that RhB degradation was significantly improved in the co-existence of PMS and catalysts. For example, approximately 79.79%, 94.28% and 90.03% of RhB were degraded in 2CoFe@PAL-500/PMS, 5CoFe@PAL-500/PMS and 8CoFe@PAL-500/PMS systems, respectively. The removal efficiency of RhB in the 2CoFe@PAL-500 system decreased because of the low concentration of the impregnation solution and less active substances on catalyst. The RhB degradation rate by 8CoFe@PAL-500 was slightly lower than that by 5CoFe@PAL, which may be due to excessive accumulation of active substances on the carrier. The active sites were generally reduced, leading to the reduced degradation rate of RhB. According to Fig. 7d, the value of k in 5CoFe@PAL-500/PMS system was the largest, indicating that the degradation rate of RhB in this system was fast. Therefore, CoFe@PAL prepared at 50 g L^{-1} of impregnation solution and 500 °C of calcination temperature is the optimum preparation conditions for PMS activation in this study.

The decomposition efficiency of PMS and TOC removal in the 5CoFe@PAL-500/PMS system was investigated and shown in Fig. 8. With the increase of PMS decomposition rate in the 5CoFe@PAL-500/PMS system, RhB was gradually degraded. After 60 min of reaction, the decomposition rates of PMS and RhB were 92.23% and 94.02%, respectively, suggesting that PMS was greatly activated by 5CoFe@PAL-500 catalyst to generate active species for RhB degradation. Moreover, the TOC removal rate was ~36.5% in the 5CoFe@PAL-500/PMS system within 60 min.

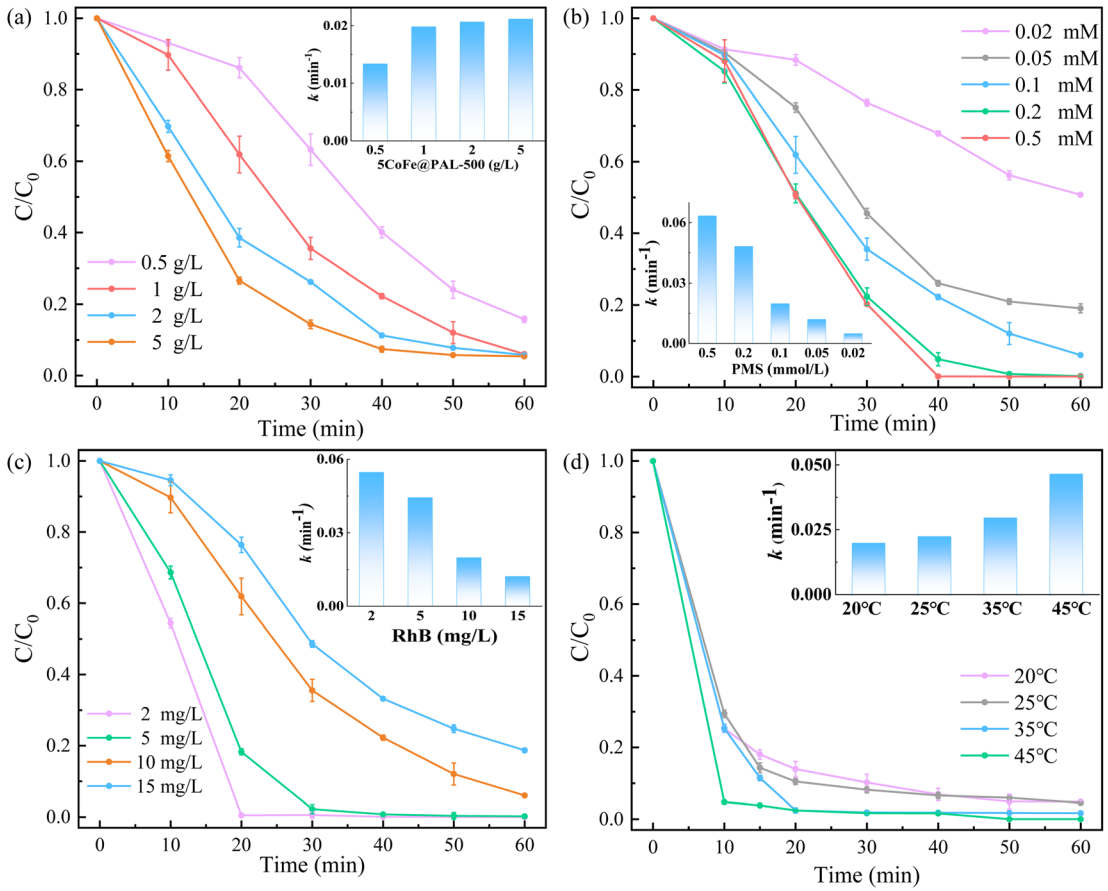

Fig. 9 (a) Effect of catalyst dosage on RhB removal ($[PMS]_0 = 0.1$ mM, $[RhB]_0 = 10$ mg L^{-1}), (b) effect of PMS dosage on RhB removal ($[RhB]_0 = 10$ mg L^{-1}, [catalyst] = 1 g L^{-1}), (c) effect of RhB concentration on RhB removal ([catalyst] = 1 g L^{-1}, $[PMS]_0 = 0.1$ mM), (d) effect of reaction temperature on RhB removal ([catalyst] = 1 g L^{-1}, $[PMS]_0 = 0.1$ mM, $[RhB]_0 = 10$ mg L^{-1}).

3.3 Removal of RhB by CoFe@PAL

3.3.1 Influence of experimental conditions. Various experimental conditions including catalyst dosage, PMS dosage, RhB concentration and reaction temperature were investigated in the catalyst/PMS system. The experimental results are shown in Fig. 9. Fig. 9a described the degradation efficiency of RhB with the increase of catalyst dosage. The RhB removal efficiency increased significantly from 84.23% to 94.28% within 60 min as the catalyst dosage from 0.5 g L^{-1} to 1.0 g L^{-1}. However, the RhB removal efficiency enhanced slightly from 94.28% to 94.64% when the catalyst dosage further increased to 5 g L^{-1} due to the fix amount of PMS in the system. The change in reaction rate constant k also complied with the tendency. Fig. 9b shows the RhB removal efficiency and reaction rate constant was improved with the increasing of PMS dosage from 0.02 mM to 0.5 mM, owning to more PMS being activated by CoFe@PAL. The effect of RhB concentration on removal efficiency in the system was investigated and the result is shown in Fig. 9c. The RhB could be completely removed in 60 min when the RhB concentration was less than 5 mg L^{-1} in the condition. It is worth noting that the RhB removal rate still reached to 94.28% at the RhB concentration of 10 mg L^{-1} and the removal rate did not drop below 81.32% until the RhB concentration reached 15 mg L^{-1}. Fig. 9d shows the effect of reaction temperature on RhB degradation. The RhB degradation efficiency increased from 95.17% to 99.99% with the increasing of temperature from 20 °C to 45 °C. The increasing reaction rate constant also shows that higher temperature can contribute to accelerate the PMS activation and generated more radicals for RhB decomposition.[31,32]

3.3.2 Influence of initial pH and co-exist substances. Initial pH is often deemed as the essential factor for catalytic degradation reactions. Fig. 10a illustrates the degradation effect of RhB at different pH values (3.0–11.0), which was adjusted by 0.1 mol L^{-1} HCl and NaOH. At pH values of 5.0–9.0, the system showed positive performance of RhB removal, and the degradation rate of RhB were 94.28%, 88.11% and 87.51% after 60 min of reaction, respectively. When the initial pH values were 3.0 and 11.0, the RhB removal rate decreased to 54.08% and 20.01%. Moreover, the k values were 0.0056, 0.0211, 0.0154, 0.0150 and 0.0016 min^{-1} at pH values of 3.0, 5.0, 7.0, 9.0 and 11.0, respectively. The results showed that the RhB degradation rate was low in strong acid or alkaline systems.

Furthermore, the pH_{pzc} of 5CoFe@PAL-500 was determined in Fig. 10b. It shows that 5CoFe@PAL-500 was positively charged at pH = 3.0. And RhB ($pK_a = 3.1$) was also in the form of cationic species at pH < 3.1.[33] Therefore, the positive electric

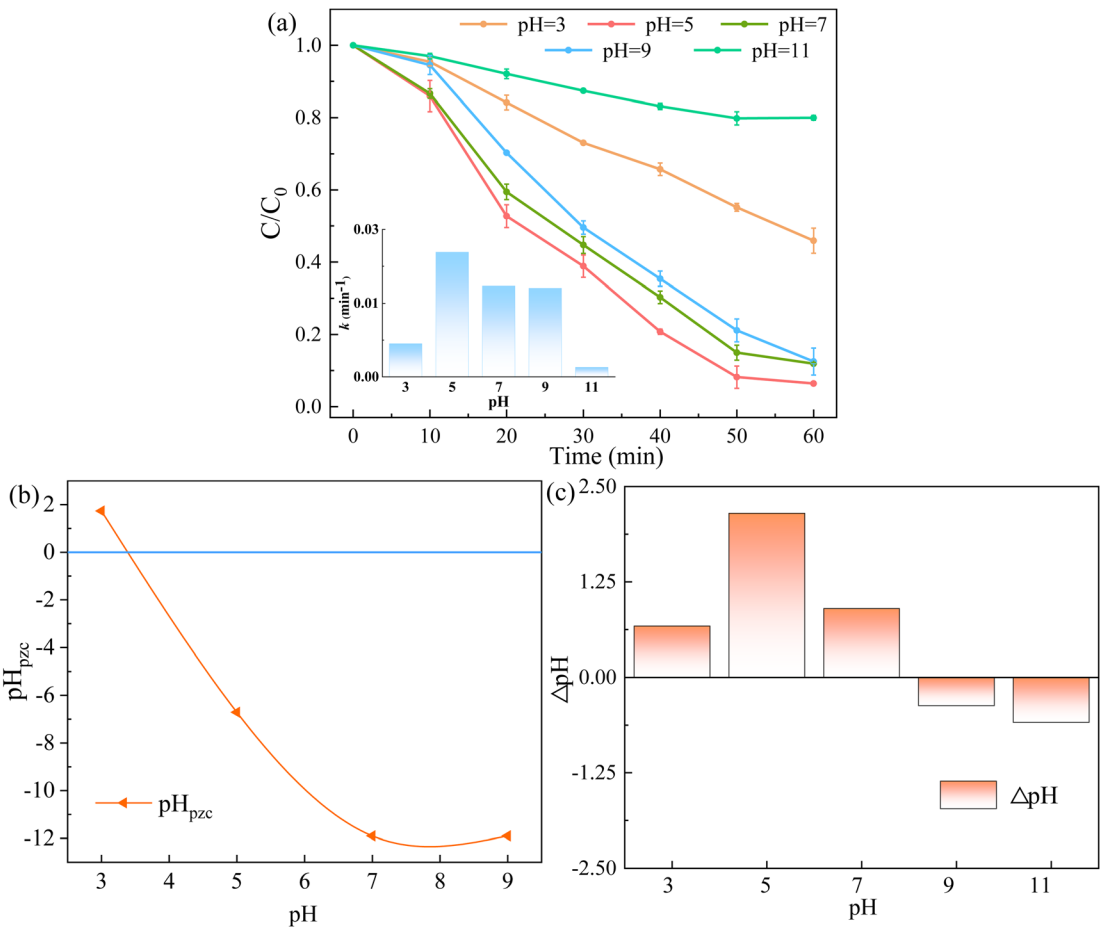

Fig. 10 (a) Effect of initial pH of solution on RhB removal, (b) the pH_{pzc} of 5CoFe@PAL-500 at different pH, (c) the final solution pH at the end of the reaction at different pH ([catalyst] = 1 g L^{-1}, $[PMS]_0$ = 0.1 mM, $[RhB]_0$ = 10 mg L^{-1}).

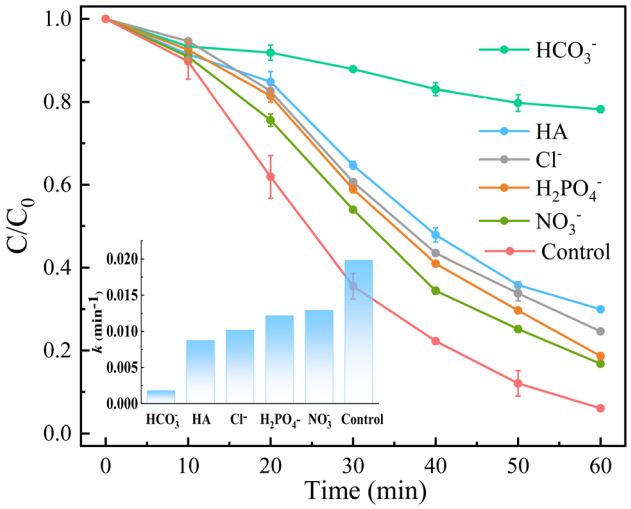

Fig. 11 Effects of anions and HA of solution on RhB removal ([catalyst] = 1 g L^{-1}, $[PMS]_0$ = 0.1 mM, $[RhB]_0$ = 10 mg L^{-1}).

repulsive forces occur between RhB and 5CoFe@PAL-500 at pH = 3.0, resulting in unfavorable performance of RhB degradation.[32] At high pH values, the generated sulfate radicals ($SO_4^{\bullet-}$) were inclined to react with the surrounding hydroxyl ions (OH^-) to form hydroxyl radicals ($^{\bullet}OH$), and followed by the conversion of $^{\bullet}OH$ into its oxygen radical ($O^{\bullet-}$) quickly (eqn (3) and (4)). Since the activity of the $O^{\bullet-}$ was much weaker than that of the $SO_4^{\bullet-}$, the RhB degradation rate became slower.[34,35] This was confirmed by the final solution pH at the end of the reaction (Fig. 10c), which showed that the pH of the final solution decreased when the initial pH of the reaction was 9.0 and 11.0.

$$SO_4^{\bullet-} + OH^- \rightarrow {}^{\bullet}OH + SO_4^{2-} \quad (3)$$

$$^{\bullet}OH + H_2O \rightarrow O^{\bullet-} + H_3O^+ \quad (4)$$

Inorganic anions and dissolved organic matter are widely present in natural water bodies. Therefore, the influences of typical inorganic anions (HCO_3^-, Cl^-, $H_2PO_4^-$ and NO_3^-) and humic acid (HA) on RhB degradation efficiency in the 5CoFe@PAL-500/PMS system were explored. As shown in Fig. 11, inorganic anions and HA showed different inhibitory effects on the 5CoFe@PAL-500/PMS system. After adding 10 mM of HCO_3^-, Cl^-, $H_2PO_4^-$ and NO_3^- into the system, the RhB degradation efficiency decreased from 94.28% to 21.78%, 75.40%, 81.36% and 83.23%, respectively. It can be attributed to

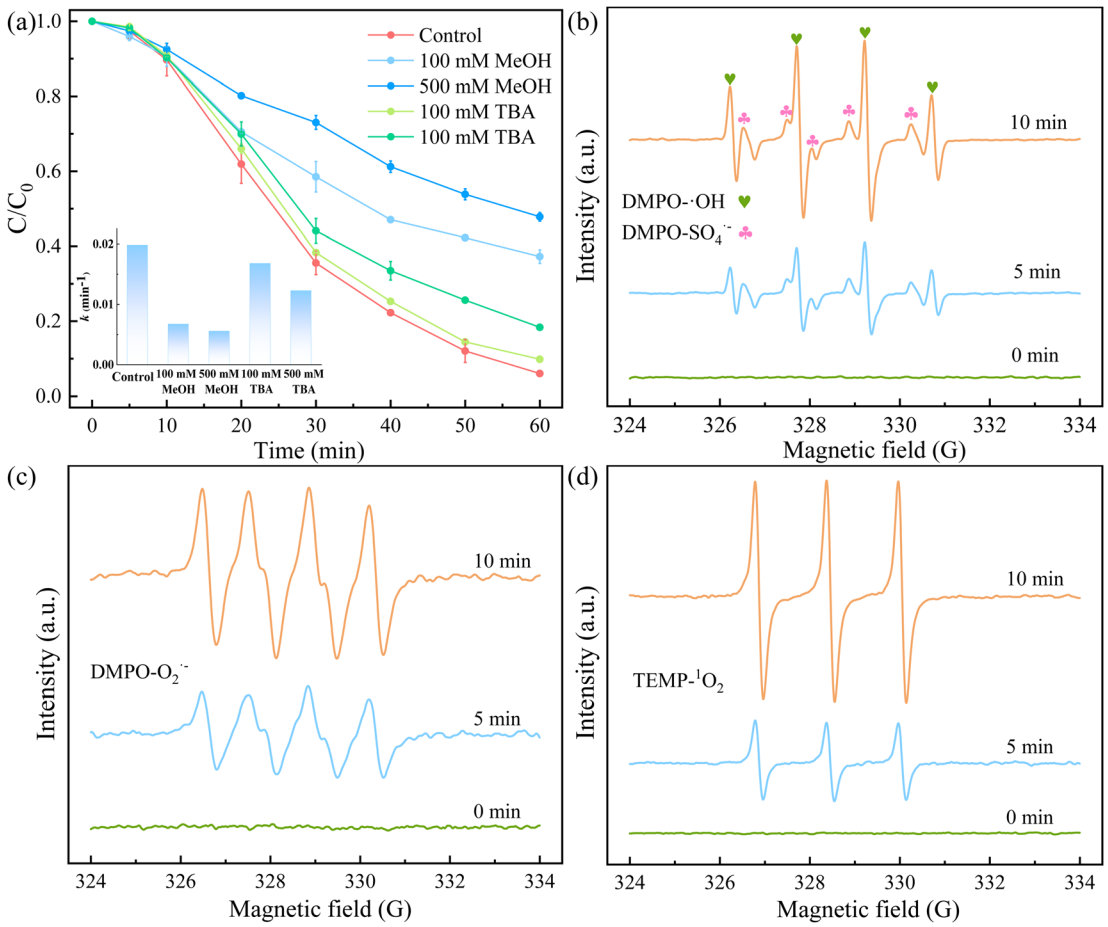

Fig. 12 (a) Effects of the radical scavengers on the RhB degradation by 5CoFe@PAL-500/PMS system, (b) EPR spectra of $^{\bullet}OH$ and $SO_4^{\bullet-}$, (c) EPR spectra of $O_2^{\bullet-}$, (d) EPR spectra of $^1O_2$ ([catalyst] = 1 g L^{-1}, $[PMS]_0$ = 0.1 mM, $[RhB]_0$ = 10 mg L^{-1}).

Table 1 Contribution of different regions in the 5CoFe@PAL-500/PMS system for RhB removal

Action of different regions	5CoFe@PAL-500 adsorption	5CoFe@PAL-500/PMS		
		$^{\cdot}OH$	$SO_4^{\cdot-}$	$O_2^{\cdot-}$ and $^1O_2$
RhB removal	14.53%	12.64%	29.47%	37.64%
Contribution percentage	15.41%	13.41%	31.26%	39.92%

the fact that HCO_3^-, Cl^-, $H_2PO_4^-$ and NO_3^- quench $^{\cdot}OH$ and $SO_4^{\cdot-}$ of the system and generating less oxidative or more selective radicals such as $CO_3^{\cdot}$, $Cl^{\cdot}$, $H_2PO_4^{\cdot}$ and $NO_3^{\cdot}$ (eqn (5)–(8)).[36] In addition, the presence of HCO_3^- increased the alkalinity of the reaction solution which resulted in the significant decrease of RhB degradation. When 10 mg L^{-1} of HA was added to the 5CoFe@PAL-500/PMS system, RhB degradation rate decreased to 70.06%. It can be attributed to the competition of HA with RhB for radicals and active sites on catalyst.[19]

$$HCO_3^- + SO_4^{\cdot-} \rightarrow CO_3^{\cdot} + SO_4^{2-} \quad (5)$$

$$Cl^- + SO_4^{\cdot-} \rightarrow Cl^{\cdot} + SO_4^{2-} \quad (6)$$

$$H_2PO_4^- + SO_4^{\cdot-} \rightarrow H_2PO_4^{\cdot} + SO_4^{2-} \quad (7)$$

$$NO_3^- + SO_4^{\cdot-} \rightarrow NO_3^{\cdot} + SO_4^{2-} \quad (8)$$

3.3.3 Identification of active species. To identify the possible active species formed in the 5CoFe@PAL-500/PMS system for RhB degradation, we conducted radical quenching tests using MeOH and TBA as radical scavengers. MeOH is a typical scavenger for $^{\cdot}OH$ ($k = 9.7 \times 10^8$ M^{-1} s^{-1}) and $SO_4^{\cdot-}$ ($k = 2.5 \times 10^7$ M^{-1} s^{-1}), and TBA is widely used as a selective radical scavenger for $^{\cdot}OH$ with the rate constant of $3.6–7.6 \times 10^8$ M^{-1} s^{-1}.[37,38] Fig. 12a illustrates the degradation efficiency of RhB in the presence of MeOH and TBA. With the addition of 100 mM TBA, the RhB degradation efficiency fell from 94.28% to 90.18%, When TBA concentration increased to 500 mM, the removal rate of RhB was further reduced to 81.64%, indicating that $^{\cdot}OH$ was involved in the catalytic reaction. In comparison to TBA, MeOH exhibited an intense inhibition effect on the removal of RhB. The RhB removal rate decreased from 62.75% to 52.17% as MeOH concentration increased from 100 mM to 500 mM. Furthermore, that the k value in the presence of MeOH was much smaller than in the presence of TBA (Fig. 12a). In conclusion, both $SO_4^{\cdot-}$ and $^{\cdot}OH$ radicals existed in the catalytic oxidation, but $SO_4^{\cdot-}$ radicals played a major role in RhB degradation.

In addition, to further identify the active species generated in the 5CoFe@PAL-500/PMS system, DMPO was taken as the spin-trapping agents to capture signals of $^{\cdot}OH$, $SO_4^{\cdot-}$, and $O_2^{\cdot-}$ by EPR. As shown in Fig. 12b, the characteristic signals for DMPO–$^{\cdot}OH$ (with a typical 1:2:2:1 quartet peak) and DMPO–$SO_4^{\cdot-}$ adducts were simultaneously observed in the system, indicating that $^{\cdot}OH$ and $SO_4^{\cdot-}$ were generated during the activation of PMS by 5CoFe@PAL catalyst. Fig. 12c shows that $O_2^{\cdot-}$ (with a typical 1:1:1:1 quartet peak) was also detected in the system. Utilizing TEMP as the trapping agent, a typical 1:1:1 triplet peak of the $^1O_2$ signal was observed in the system (Fig. 12d).[8,27,32] The above results show that $^{\cdot}OH$, $SO_4^{\cdot-}$, $O_2^{\cdot-}$

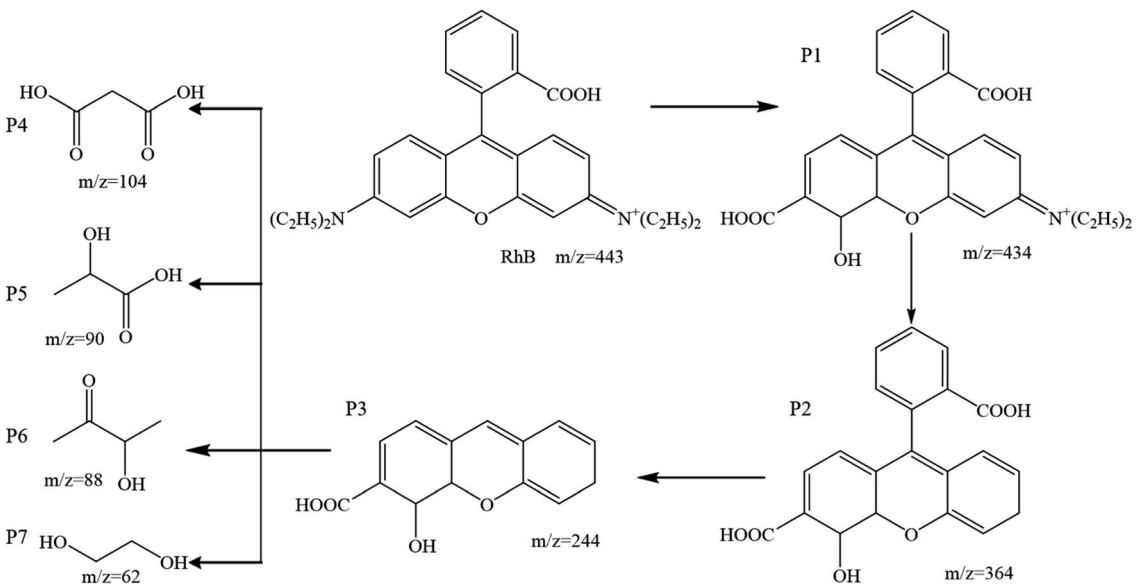

Fig. 13 The possible degradation pathway of RhB in the 5CoFe@PAL-500/PMS system ([catalyst] = 1 g L^{-1}, $[PMS]_0$ = 0.1 mM, $[RhB]_0$ = 10 mg L^{-1}).

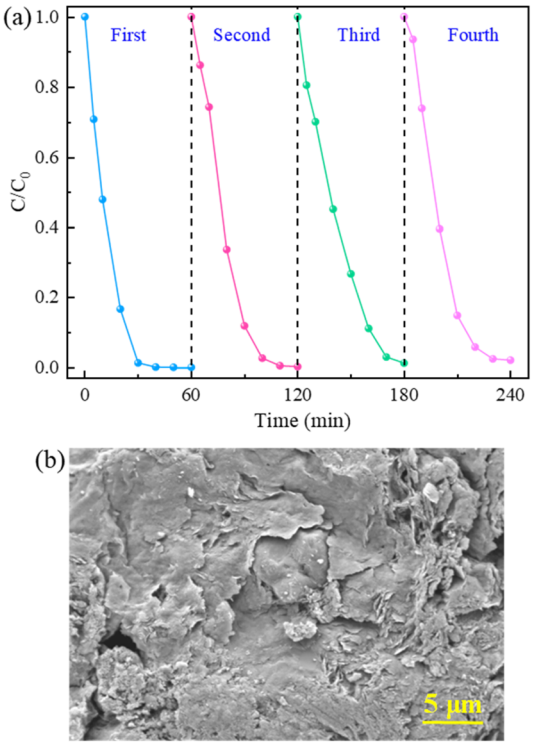

Fig. 14 (a) RhB removal in the reusability tests, (b) SEM image of 5CoFe@PAL-500 after repeated tests ([catalyst] = 2 g L^{-1}, $[PMS]_0$ = 0.2 mM, $[RhB]_0$ = 10 mg L^{-1}).

and $^1O_2$ radicals co-participated in the RhB degradation in the 5CoFe@PAL/PMS system.

According to Fig. 7 and 12a, the contribution of different pathways was evaluated for RhB removal in the 5CoFe@PAL-500/PMS system (Table 1). The adsorption contribution of 5CoFe@PAL-500 for RhB within 60 min was 15.41%. And the oxidative decomposition contribution of $SO_4^{\cdot-}$ and $^{\cdot}OH$ for RhB was 13.41% and 31.26%, respectively. Additionally, the total oxidative decomposition contribution of $O_2^{\cdot-}$ and $^1O_2$ for RhB was 39.92%.

3.3.4 Degradation pathway of RhB. The intermediates during RhB degradation in the 5CoFe@PAL-500/PMS system were analyzed by LC-MS and the detailed information are given in Fig. 13. According to the identified chemical structures, seven intermediates were detected in the system. Based on the identified intermediates and reported studies, the proposed degradation pathway of active species attacking RhB to produce intermediates is attributed to the deethylation, chromophore cleavage and the opening of benzene ring.[39,40] Eventually, the intermediates would further be attacked by the radicals and oxidized to CO_2 and H_2O.

3.3.5 Stability and reusability of catalyst. The stability and reusability of 5CoFe@PAL-500 were evaluated by four-cycle tests. After each catalytic degradation experiment, the catalyst was recovered from the solution by filtration, then washed with DI water several times and finally dried in an oven at 70 °C for the next test. As depicted in Fig. 14a, the degradation rate of RhB still remained above 97% within 60 min in four replicate tests. At the same time, Fig. 14b shows the SEM image of used CoFe@PAL. The result indicates that some cobalt iron oxide was still immobilized on the PAL surface after repeated use. Furthermore, Table 2 shows that the mass of catalyst changed slightly after four repeated experiments, only reduced by 0.02 g. The above results indicated that 5CoFe@PAL-500 exhibited excellent stability and reusability for RhB degradation.

Table 2 Weight change of 5CoFe@PAL-500 after repeated test

Cycle index	Initial	First	Second	Third	Fourth
Quality/g	0.2077	0.1864	0.1822	0.1791	0.1784
Quality loss/%		7.12	9.21	10.76	11.11
Quality loss/g		0.0143	0.0185	0.0216	0.0223

4. Conclusions

In summary, the CoFe@PAL catalyst was successfully synthesized as a PMS activator for RhB removal. The CoFe@PAL exhibited the best catalytic performance for RhB degradation with 50 g L^{-1} of impregnation solution and 500 °C of calcination temperature. The optimized catalyst showed the efficiency of 94.28% within 60 min for RhB removal. In addition, the 5CoFe@PAL-500/PMS system showed the excellent capability of RhB removal at pH range of 5–9. Compared to other inorganic anions, HCO_3^- had a greater influence on the degradation effect in the system. The radical quenching experiments and EPR characterization revealed that $^{\cdot}OH$, $SO_4^{\cdot-}$, $O_2^{\cdot-}$ and $^1O_2$ radicals existed in the 5CoFe@PAL-500/PMS system simultaneously. The LC-MS analysis results indicated that the primary degradation mechanisms of RhB were deethylation, chromophore cleavage, and benzene ring opening. Finally, cycle experiments and SEM characterization proved that 5CoFe@PAL-500 maintained good stability and reusability. In conclusion, the resultant 5CoFe@PAL-500 is a promising catalyst for PMS activation and degradation of organic pollutants in aqueous solution.

Conflicts of interest

There are no conflicts to declare.

Acknowledgements

This work was supported by the National Natural Science Foundation of China (No. 52100010), the Key-Area Research and Development Program of Guangdong Province (No. CF872022000068), the Natural Science Foundation of Shandong Province (No. ZR2020ME256 and ZR2021QE185) and the Fund of Fujian Provincial Key Laboratory of Marine Ecological Conservation and Restoration (EPR2020009).

References

1 Y. Zhang, Q. Yang, J. Liang, Y. Luo, Q. Liu, Y. Yang and X. Sun, *J. Solid State Chem.*, 2022, **169**, 110893.

2 A. Y. Sham and S. M. Notley, *J. Environ. Chem. Eng.*, 2018, **6**, 495–504.
3 T. Depci, A. R. Kul and Y. Önal, *Chem. Eng. J.*, 2012, **200**, 224–236.
4 H. Ni, M. Arslan, J. Wei, J. Dai, Z. Luo, R. Cai, S. Zhao, M. G. El-Din and Z. Wu, *Sci. Total Environ.*, 2021, **785**, 147272.
5 Y. Fan, Y. Ji, D. Kong, J. Lu and Q. Zhou, *J. Hazard. Mater.*, 2015, **300**, 39–47.
6 X. Duan, Z. Ao, H. Sun, L. Zhou, G. Wang and S. Wang, *Chem. Commun.*, 2015, **51**, 15249–15252.
7 Q. Yang, Y. Yang, Y. Zhang, L. Zhang, S. Sun, K. Dong, Y. Luo, J. Wu, X. Kang and Q. Liu, *Chemosphere*, 2023, **311**, 137020.
8 X. Li, Z. Wang, B. Zhang, A. I. Rykov, M. A. Ahmed and J. Wang, *Appl. Catal., B*, 2016, **181**, 788–799.
9 X. Duan, C. Su, J. Miao, Y. Zhong, Z. Shao, S. Wang and H. Sun, *Appl. Catal., B*, 2018, **220**, 626–634.
10 A. Rastogi, S. R. Al-Abed and D. D. Dionysiou, *Appl. Catal., B*, 2009, **85**, 171–179.
11 G. P. Anipsitakis, D. D. Dionysiou and M. A. Gonzalez, *Environ. Sci. Technol.*, 2006, **40**, 1000–1007.
12 G. P. Anipsitakis and D. D. Dionysiou, *Environ. Sci. Technol.*, 2003, **37**, 4790–4797.
13 Q. Yang, Y. Zhang, J. Liang, Y. Luo, Q. Liu, Y. Yang and X. Sun, *Colloids Surf., A*, 2022, **648**, 129239.
14 P. R. Shukla, S. Wang, H. Sun, H. M. Ang and M. Tadé, *Appl. Catal., B*, 2010, **100**, 529–534.
15 Y. Luo, C. Liu, T. Mehmood, Y. Zhang, M. Yu and Y. Ren, *J. Environ. Chem. Eng.*, 2021, **9**, 106036.
16 Y. Ren, L. Lin, J. Ma, J. Yang, J. Feng and Z. Fan, *Appl. Catal., B*, 2015, **165**, 572–578.
17 Y. Zhang, Q. Yang, L. Yue, Q. Liu, Y. Luo, J. Wu, X. Kang, S. Sun, Y. Yang and X. Sun, *J. Water Process Eng.*, 2023, **51**, 103324.
18 R. Xie, J. Ji, H. Huang, D. Lei, R. Fang, Y. Shu, Y. Zhan, K. Guo and D. Y. Leung, *Chem. Eng. J.*, 2018, **341**, 383–391.
19 X. Lei, M. You, F. Pan, M. Liu, P. Yang, D. Xia, Q. Li, Y. Wang and J. Fu, *Chin. Chem. Lett.*, 2019, **30**, 2216–2220.
20 T. Warang, N. Patel, R. Fernandes, N. Bazzanella and A. Miotello, *Appl. Catal., B*, 2013, **132**, 204–211.
21 L. Chen, S. Yang, X. Zuo, Y. Huang, T. Cai and D. Ding, *Chem. Eng. J.*, 2018, **354**, 856–865.
22 X. Li, H. Shi, W. Zhu, S. Zuo, X. Lu, S. Luo, Z. Li, C. Yao and Y. Chen, *Appl. Catal., B*, 2018, **231**, 92–100.
23 G. Tian, W. Wang, L. Zong, Y. Kang and A. Wang, *Chem. Eng. J.*, 2016, **293**, 376–385.
24 X. Li and K. Peng, *Appl. Clay Sci.*, 2018, **162**, 175–181.
25 B. Saravanakumar, S. Ramachandran, G. Ravi, V. Ganesh, R. K. Guduru, A. Sakunthala and R. Yuvakkumar, *J. Nanosci. Nanotechnol.*, 2020, **20**, 96–105.
26 L.-L. Shen, K. Xia, W.-Z. Lang, L.-F. Chu, X. Yan and Y.-J. Guo, *Chem. Eng. J.*, 2017, **324**, 336–346.
27 C. Chen, L. Liu, Y. Li, W. Li, L. Zhou, Y. Lan and Y. Li, *Chem. Eng. J.*, 2020, **384**, 123257.
28 S. Guo, Z. Yang, H. Zhang, W. Yang, J. Li and K. Zhou, *J. Mater. Sci. Technol.*, 2021, **62**, 34–43.
29 Z. Zhou, Y. Zhang, Z. Wang, W. Wei, W. Tang, J. Shi and R. Xiong, *Appl. Surf. Sci.*, 2008, **254**, 6972–6975.
30 X.-H. Yi, T.-Y. Wang, H.-Y. Chu, Y. Gao, C.-C. Wang, Y.-J. Li, L. Chen, P. Wang, H. Fu and C. Zhao, *Chem. Eng. J.*, 2022, **449**, 137784.
31 H. Fu, S. Ma, P. Zhao, S. Xu and S. Zhan, *Chem. Eng. J.*, 2019, **360**, 157–170.
32 P. Duan, T. Ma, Y. Yue, Y. Li, X. Zhang, Y. Shang, B. Gao, Q. Zhang, Q. Yue and X. Xu, *Environ. Sci.: Nano*, 2019, **6**, 1799–1811.
33 F. López Arbeloa, T. López Arbeloa, M. Tapia Estévez and I. López Arbeloa, *J. Chem. Phys.*, 1991, **95**, 2203–2208.
34 L. Gan, Q. Zhong, A. Geng, L. Wang, C. Song, S. Han, J. Cui and L. Xu, *Sci. Total Environ.*, 2019, **694**, 133705.
35 L. Xu, W. Chu and L. Gan, *Chem. Eng. J.*, 2015, **263**, 435–443.
36 S. Wang, Q. Wu, R. Huang, Y. Guo, B. Yan, X. Hao, J. Li, W. Xia and J. Tian, *J. Water Process Eng.*, 2022, **47**, 102751.
37 S. Wang, Q. Wu, B. Yan, Y. Guo, W. Xia, J. Li, F. Cui and J. Tian, *Sep. Purif. Technol.*, 2022, **291**, 120874.
38 F.-X. Wang, Z.-C. Zhang, X.-H. Yi, C.-C. Wang, P. Wang, C.-Y. Wang and B. Yu, *Crystengcomm*, 2022, **24**, 5557–5561.
39 J. Shi, Z. Ai and L. Zhang, *Water Res.*, 2014, **59**, 145–153.
40 Y. Wang, F. Li, T. Xue, C. Liu, D. Yuan, F. Qi and B. Xu, *Environ. Sci. Pollut. Res.*, 2018, **25**, 4419–4434.